Presynaptic reorganization in the sensory hair cell after noise exposure

Yan Lu[a,b,c,d], Shengxiong Wang[d], Haoyu Wang[d], Fangfang Wang[d], Hua Han[e,f,g], Jing Liu[e,1], Yunfeng Hua[a,b,c,d,1]

[a]Department of Otolaryngology-Head and Neck Surgery, Shanghai Ninth People's Hospital, Shanghai, China

[b]Ear Institute, Shanghai Jiao Tong University School of Medicine, Shanghai, China

[c]Shanghai Key Laboratory of Translational Medicine on Ear and Nose Diseases, Shanghai, China

[d]Shanghai Institute of Precision Medicine, Ninth People's Hospital, Shanghai Jiao Tong University School of Medicine, Shanghai, China

[e]National Laboratory of Pattern Recognition, Institute of Automation, Chinese Academy of Sciences, Beijing, China

[f]School of Artificial Intelligence, School of Future Technology, University of Chinese Academy of Sciences, Huairou District, Beijing, China

[g]CAS Center for Excellence in Brain Science and Intelligence Technology, Shanghai, China

[1]To whom correspondence may be addressed. Email: liujing2016@ia.ac.cn (J.L.) or yunfeng.hua@shsmu.edu.cn (Y.H.)

Running title

Presynaptic reorganization in the IHC

Keywords

cochlear synaptopathy/ inner hair cell/ ribbon morphology/ synaptic mitochondria

Abstract

In mammals, neural encoding of sounds is mediated by ribbon-type synapses between inner ear hair cells (IHCs) and postsynaptic spiral ganglion neurons. These specialized connections are arranged along the IHC basolateral surface with gradient changes in morphology and electrophysiological properties, which are essential for the level coding of sound intensity. Large synaptic ribbons, which predominantly reside on the modiolar IHC face, are responsive to loud sounds and more susceptible to acoustic insults. Selective loss of them is the major cause for reduced cochlear audible range. However, other than fewer ribbons after noise exposure, the consequential presynaptic reorganization in the IHCs remains less characterized. Here, by means of volume electron microscopy and artificial intelligence-assisted image analysis, we investigated noise exposure-related changes in the mouse IHCs. Apart from morphological changes of the ribbon-type active zones, our quantifications reveal differential synaptic reorganization and mitochondrial remodeling in an IHC subtype-specific manner. Together, these results argue for putative presynaptic mechanisms underlying activity-dependent structural changes of synaptic ribbons and the associated mitochondrial network (which powers the neurotransmission) in the sensory epithelial cells.

43 **Introduction**

44 In the mammalian cochlea, sounds are decomposed into different frequency components
45 by the basilar membrane (BM), establishing a place-frequency map for resident sensory
46 epithelial cells – the inner hair cells (IHCs) – as well as postsynaptic spiral ganglion neurons
47 (SGNs) (for reviews, see (Fettiplace, 2017; Huet et al, 2019; Moser et al, 2020)). In rodents
48 for instance, each IHC is contacted by about 20 predominantly unbranched peripheral
49 dendrites of the type I SGNs, forming up to 25 active zones (AZs) with characteristic
50 electron-dense and vesicle-tethering synaptic ribbons. These specialized connections are
51 proven of an essential role for ultrafast and temporally-precise sound encoding (for reviews,
52 see (Moser et al., 2020; Safieddine et al, 2012)). Early studies using light (Frank et al, 2010;
53 Liberman et al, 2011; Liberman et al, 1990; Meyer et al, 2009; Wong et al, 2014) and
54 electron microscopy (Bullen et al, 2015; Hua et al, 2021; Liberman et al., 1990; Michanski et
55 al, 2019; Payne et al, 2021) have revealed great diversity in both pre- and postsynaptic
56 morphology of the ribbon synapses. They are found arranging in a spatial gradient with
57 large ribbons on the modiolar (neural) IHC face whereas small ones on the pillar (abneural)
58 face. Such morphological heterogeneity has been proposed of crucial functional implications,
59 as the ribbon-bound synaptic vesicle (SV) pool increases with expanding ribbon volume
60 (Michanski et al., 2019; Payne et al., 2021; Stamataki et al, 2006) and thus more fusion-
61 competent SVs are made available to the synaptic release site (Joselevitch & Zenisek, 2020;
62 Vaithianathan et al, 2016). Moreover, ribbons of different size are presumably aligned to
63 three distinct functional and molecular SGN subtypes (Petitpre et al, 2018; Shrestha et al,
64 2018; Sun et al, 2018). A prevailing view on such divergent connectivity pattern of afferent
65 connections is to enable collectively neural encoding of the entire audible range by the

66 functionally fractionated SGNs (Heil & Peterson, 2015; Moser et al., 2020; Pangrsic et al,
67 2018).

68 In the mature cochlea however, these fine-structured afferent connections are
69 found most susceptive to acoustic insults and non-regenerative once lost. Even moderate
70 overexposure can lead to a permanent ribbon loss of up to ~50 % and subsequent SGN
71 death in the rodent models (Kujawa & Liberman, 2009; Liberman et al, 2015), providing a
72 plausible explanation for significant reduction in the synaptic counts observed in elder
73 mammals (Fernandez et al, 2015; Sergeyenko et al, 2013) including human (Wu et al, 2019).
74 In addition to ribbon loss (also known as cochlear synaptopathy), the IHCs appear to have
75 difficulty in maintaining a prominent ribbon gradient following noise exposure. In
76 accordance with this observation, selective damage occurs on those large modiolar ribbons
77 (Furman et al, 2013; Liberman et al., 2015), to which the postsynaptic terminals are believed
78 more vulnerable to glutamate excitotoxicity (see review (Liberman, 2017)). Therefore,
79 coding deficits, as a causal consequence of the cochlear synaptopathy, are likely implicated
80 in the weakened auditory discrimination under background noise, which is one of the
81 hallmarks of hidden hearing loss and presbycusis (Kujawa & Liberman, 2015; Shi et al, 2016).

82 Although post-exposure dynamics of the cochlear synaptopathy has been
83 extensively studied using light microscopy (LM) in different species (Fernandez et al., 2015;
84 Hickman et al, 2020; Liberman et al., 2015; Shi et al., 2016), quantitative structural
85 investigations at higher spatial resolution and with comprehensive cellular context are
86 needed for understanding the presynaptic concepts for adaptive ribbon plasticity and
87 reorganization. Most recent advances in three-dimensional (3D) electron microscopy (EM)
88 and artificial intelligence-based segmentation techniques have made it possible to volume
89 reconstruct the IHCs at unprecedent large scale and superior resolution (Bullen et al., 2015;

90 Hua et al., 2021; Liu et al, 2022; Michanski et al., 2019; Payne et al., 2021). Here, we
91 employed serial block-face scanning electron microscopy (SBEM) to capture presynaptic
92 structural changes in six large datasets of the cochlea, which were acquired from middle and
93 basal turns of juvenile mice with or without acoustic overexposure history. Specifically, we
94 quantified morphology and distribution of the ribbon-type AZs in pooled and grouped IHCs
95 following synaptopathic and non-synaptopathic exposure, as well as attempted to
96 characterize the putative ribbon-associated mitochondrial network and its synaptic activity-
97 dependent remodeling.
98

Results

SBEM Imaging of Noise Exposed Cochlear Organ of Corti. In this study, we acquired six SBEM datasets of cochlea from four male CBA mice at 5-6 weeks of age (Fig 1A). The imaged volumes are centered on the organs of Corti and each contains 18.7 ± 4.0 IHCs (see Table 1 for more dataset information). Among these are two control datasets from individual animals without noise-exposure history (M1/2, taken from basal cochlear turn), whereas four from the other two animals (M3/4, taken from both middle and basal turns) on the post-exposure day-7 to a two-hour (2 h) pure tone of 8-16 kHz at 91-dB sound pressure level (SPL). The use of this narrowband noise frequency has been previously well established and yields temporary hearing loss with distinct frequency characters in an exposure dose-dependent manner (Fernandez et al., 2015; Kujawa & Liberman, 2009; Liberman et al., 2015). Auditory brainstem responses (ABRs) of the exposed animals confirmed transient hearing threshold elevations upon the so-called synaptopathic (91-dB, 2 h) as well as non-synaptopathic (85-dB, 2 h) sounds (Fig 1B and C). Specifically, the peak threshold elevation of the 85-dB exposed group was at 22.6 kHz (30.00 ± 1.05 dB, n = 10) in terms of ABR test frequencies on the post-exposure day one (D1), whereas the 91-dB exposed group demonstrated a monotonically increased threshold elevation with the test frequency starting from 8 kHz and reaching a maximum at 45.2 kHz (32.86 ± 1.38 dB, n = 7). On the post-exposure day seven (D7), a full recovery in the ABR thresholds was observed in both exposed groups (Fig 1B and C), suggesting the absence of a permanent hearing loss. Note that there is an age-related difference in the noise susceptibility between the mature (> 8 weeks) and our juvenile (5-6 weeks) CBA mice (see Discussion).

To implement targeted trimming of the cochlea samples prior to SBEM acquisition, we first acquired X-ray tomographic data from the stained and resin-embedded sample

123 blocks (Fig 1D). This allowed corresponding the cochlear anatomical features observed from
124 tissue block-faces and virtual cross-sections on the tomographic reconstructions (Fig 1E).
125 Based on the standard place-frequency relationship of the mouse cochlea (Muller et al,
126 2005), we were able to narrow down the best-frequency range of the middle- and basal-
127 turn SBEM volumes (Fig 1F and Appendix Fig S1, 16.2 ± 0.8 kHz and 28.1 ± 1.0 kHz) according
128 to determined anatomical positions. Within these two fixed tonotopic places (16 kHz and 28
129 kHz), we set out to focus on IHC structural comparisons after the synaptopathic exposure
130 (91-dB, 2 h).
131
132 **Enlarged and Multi-ribbons after Acoustic Overexposures.** Using the established image
133 analysis pipeline powered by artificial intelligence (Liu et al., 2022), we volume
134 reconstructed 112 intact IHCs and all 1710 basolateral pole-resided ribbon synapses in the
135 SBEM datasets (Fig 2A and Table 1). As spatial resolution of the SBEM enabled capturing of
136 different ribbon morphologies including multi-ribbons (Fig 2B), we set out to characterize
137 the exposure-related changes of the IHC ribbons. In good agreement with prior LM studies
138 (Fernandez et al., 2015; Grierson et al, 2022; Kujawa & Liberman, 2009; Liberman et al.,
139 2015), a substantial ribbon loss (29.4 %) was observed in the 28 kHz cochlear region
140 following the 91-dB exposure (Fig 2C, 91-dB: 12.0 ± 2.9, n = 46 IHCs) in comparison with the
141 unexposed control group (ctl: 17.0 ± 1.9, n = 33 IHCs, $p < 0.0001$). In the middle (16 kHz)
142 cochlear region, where the 91-dB exposure caused a comparable ABR threshold shift to that
143 of the 28 kHz region, slightly more ribbons per IHC were observed (Fig 2C, 91-dB: 18.1 ± 1.8,
144 n = 33 IHCs, $p = 0.0171$) presumably due to cochlear region-specific difference. These results
145 are consistent to numerous early observations, arguing for a noise-induced ribbon change
146 specifically at high frequency-responsive basal segment of the cochlear BM.

147 Similarly, following the exposures the IHCs tended to have enlarged ribbons in the 28
148 kHz-region (Fig 2D, ctl: 0.0129 ± 0.0004 μm^3, n = 33 IHCs; 91-dB: 0.0184 ± 0.0008 μm^3, n = 46
149 IHCs, $p < 0.0001$), but not in the 16 kHz-region from the same samples (91-dB: 0.0130 ±
150 0.0002 μm^3, n = 33 IHCs, p = 0.7320). The observed volume change was unlikely caused by
151 acute hollowing of synaptic ribbon based on its low occurrence in our datasets (Appendix
152 Fig S2A). Alternatively, additional multi-ribbon AZs might also account for this post-exposure
153 ribbon enlargement, as cumulative ribbon volume was measured on individual AZs,
154 irrespective of single or multiple ribbons (Fig 2B). In fact, we did notice a slight but
155 statistically significant increase in the occurrence of multi-ribbon AZs after the 91-dB
156 exposure (Fig 2E, ctl: 1.70 ± 1.19, n = 33 IHCs; 91-dB: 2.46 ± 1.24, n = 46 IHCs, p = 0.0078),
157 but those IHCs with severe synaptopathy do not necessarily have more multi-ribbon AZs (Fig
158 2E), arguing against the notion that the multi-ribbon AZ is a byproduct of the synaptopathy
159 or a major contributor to the ribbon enlargement. Nevertheless, the cumulative ribbon
160 volume per IHC seemed to be relatively stable in spite of the noise-induced synapse loss
161 (Appendix Fig S2B, ctl: 0.217 ± 0.033 μm^3, n = 33 IHCs; 91-dB: 0.208 ± 0.044 μm^3, n = 46 IHCs,
162 p = 0.3157). Furthermore, an increase in ribbon size heterogeneity was noted in pooled AZs
163 following the synaptopathic exposure (Fig 2F), probably owing to high percentage of the
164 enlarged and multi-ribbons. Besides, the IHC pillar-modiolar gradient of ribbon size was
165 compromised by the exposure (Appendix Fig S2C). Together, these results provide new
166 ultrastructural insights in adaptive plasticity changes of the IHC ribbons.
167
168 **Differential Synaptopathy in the IHCs upon Noise Damage.** It has been recently showed
169 that the staggered mid-cochlea IHCs can be subdivided into two distinct morphological
170 subtypes (Liu et al., 2022; Yin et al, 2014). In both 16 kHz- and 28 kHz-region, we confirmed

171 the copresence of the pillar cell-oriented (type-A) as well as the modiolus-oriented (type-B)
172 subpopulations with opposing ribbon density gradients along the IHC pillar-modiolus axis
173 (Fig 3A). Given that the postsynaptic SGNs with molecular diversity are arranged with
174 distinct spatial preferences (Petitpre et al., 2018; Shrestha et al., 2018; Sun et al., 2018),
175 such alternating IHC basolateral pole positions can be of functional relevance via
176 introducing disproportionated ribbon synapse compositions and thereby differentiate the
177 IHC receptive field of sound intensity (Liu et al., 2022). We then asked whether these two
178 IHC subtypes responded to acoustic insults differently in terms of post-exposure ribbon loss
179 and reorganization.

180 In the 28 kHz-region, the type-A IHCs appeared more alike those located at the
181 cochlear apex, featuring a prominent modiolar-pillar gradient in ribbon size and abundance
182 (Liberman et al., 2011). The post-exposure changes in the type-A IHC ribbons were found
183 exclusively on the modiolar face (Fig 3B, ctl: 10.9 ± 2.2, n = 21 IHCs; 91-dB: 6.9 ± 2.2, n = 30
184 IHCs, $p < 0.0001$), where commonly the ribbon synapses were densely packed. By contrast,
185 their pillar ribbons were more robust to the exposure (Fig 3B, ctl: 6.1 ± 1.6, n = 21 IHCs; 91-
186 dB: 5.6 ± 1.5, n = 30 IHCs, $p = 0.2165$). However, the post-exposure enlargement of the type-
187 A IHC ribbons occurred not only on the modiolar face (Fig 3C, ctl: 0.0142 ± 0.0005 μm^3, n
188 =21 IHCs; 91-dB: 0.0171 ± 0.0008 μm^3, n = 30 IHCs, $p = 0.0088$), but also on the pillar face
189 (ctl: 0.0091 ± 0.0004 μm^3, n = 21 IHCs; 91-dB: 0.0150 ± 0.0008 μm^3, n = 30 IHCs, $p < 0.0001$),
190 which effectively compromised the ribbon size gradient. Besides, the ribbon loss in the 91-
191 dB group resulted in an increased inter-distance of the modiolar ribbons (Fig 3D, ctl: 2.16 ±
192 0.08 µm, n = 21 IHCs; 91-dB: 2.98 ± 0.16 µm, n = 30 IHCs, $p = 0.0002$), diminishing the
193 normal ribbon density gradient along IHC modiolar-pillar axis (ctl: 2.16 ± 0.08 µm versus
194 3.36 ± 0.13 µm, n = 21 IHCs, $p < 0.0001$; 91-dB: 2.98 ± 0.16 µm versus 3.44 ± 0.15 µm, n = 30

195 IHCs, p = 0.0682). These results from the type-A IHCs conform the long-lasting dogma with
196 respect to the modiolar ribbons being more vulnerable to acoustic insults (Liberman et al.,
197 2015).

198 As counterparts, the type-B IHCs appeared to have few but robust modiolar ribbons
199 (Fig 3B, ctl: 3.8 ± 1.2, n = 12 IHCs; 91-dB: 2.3 ± 1.6, n = 16 IHCs, p = 0.0145), while the noise-
200 related changes took place predominantly on the pillar face in terms of reduced ribbon
201 number (Fig 3B, ctl : 13.2 ± 2.1, n = 12 IHCs; 91-dB: 8.7 ± 3.2, n = 16 IHCs, p = 0.0003) and
202 enlarged mean size (Fig 3C, ctl: 0.0134 ± 0.0007 μm^3, n = 12 IHCs; 91-dB: 0.0210 ± 0.0015
203 μm^3, n = 13 IHCs, p = 0.0002). Note that the modiolar preference of ribbons seemed to be
204 maintained in the type-B IHCs following the exposure (Fig 3D, ctl: 3.72 ± 0.38 µm versus 2.41
205 ± 0.08 µm, n = 12 IHCs, p = 0.0048; 91-dB: 3.89 ± 0.37 µm versus 2.80 ± 0.18 µm, n = 11 IHCs,
206 p = 0.0269) in spite of significant ribbon loss and volume change. Together, these results
207 enrich our current view on noise damage in the mid-basal cochlear regions by revealing a
208 set of differences in the post-exposure ribbon organization between two IHC subtypes,
209 which are thought to be equivalently activated upon sensory stimuli.

210

211 **Activity-dependent Remodeling of Synaptic Mitochondrial Network.** In the IHC basolateral
212 compartment, a distance-dependent correlation between the spatial gradient of ribbons
213 and nearby mitochondria was recently reported (Liu et al., 2022). It, however, remains
214 elusive whether the IHC mitochondrial network is adaptively remodeled to the plasticity
215 changes of ribbons. To address this question, the modiolar volume fractions of ribbons and
216 mitochondria were used to compute the correlation coefficients within a domain of growing
217 size from the IHC basolateral pole (Fig 4A and B1). Compared to the unexposed control
218 group, the 91-dB exposure caused an overall reduction in the ribbon-mitochondrion

219 correlation but with similar distance-dependence in the synaptopathic 28 kHz-region
220 (Fig 4B2). Note that the maximum correlations were constantly observed between ribbons
221 and mitochondria within 5 µm from the IHC basal pole (Fig 4B2), implying a strong interplay
222 between ribbons and the adjacent mitochondria. We thereby, nicknamed this anatomical
223 subpopulation as "ribbon-associated mitochondria" or "RAM". Further, we show that the
224 RAM constitute about 17 % of total mitochondria in the basal IHC compartment (Fig 4B3, ctl:
225 17.12 ± 5.70 %, n = 33 IHCs; 91-dB: 15.69 ± 5.72 %, n = 46 IHCs, p = 0.2760). We controlled
226 that such decrease in spatial correlation was caused by redistribution of both ribbons and
227 the RAM following the exposure (Fig 4C and 4D). In addition, we observed a declined
228 fraction of large mitochondria in the pooled RAM following the 91-dB exposure (Fig 4E, ctl:
229 0.0882 ± 0.0008 μm^3, n = 4368; 91-dB: 0.0735 ± 0.0005 μm^3, n = 6065, $p < 0.0001$),
230 presumably owing to activity-dependent mitochondrial fission.
231

232 **Discussion**

233 Mechanosensory hair cells are multi-functionally compartmentalized with specialized
234 organelles, making them attractive model systems for studying the interplay
235 between/among subcellular components including ribbon synapses, synaptic vesicles,
236 mitochondria and membrane cisterns (Chakrabarti et al, 2018; Esterberg et al, 2014;
237 Hashimoto et al, 1990; Kantardzhieva et al, 2013; Lioudyno et al, 2004; Lysakowski &
238 Goldberg, 1997; Spicer et al, 2007; Spicer et al, 1999). By the aid of advanced techniques in
239 serial sectioning, electron microscopy (EM) reconstruction at whole-cell level has become
240 much less labor intensive, contributing to the discoveries of key morphological hallmarks in
241 developing (Michanski et al., 2019; Payne et al., 2021), mature (Bullen et al., 2015; Dow et al,
242 2015; Hua et al., 2021), aging (Lauer et al, 2012), as well as noise-injured (Bullen et al, 2019)
243 sensory organs.

244 For this study the SBEM is our method of the choice because it is advantageous over
245 other 3D EM as well as LM methods in visualizing large-scale IHC ultrastructure. Sufficient
246 tissue size is critical for determining global orientation of the IHCs by referencing to other
247 cochlear structures, whereas nanometer resolution of the SBEM allows identifying outlines
248 of individual IHC bodies in densely packed regions. These enable comprehensive mapping
249 morphology and cellular distribution of ribbons, especially in the case of noise-damaged
250 IHCs containing orphan and "hollow" ribbons (Liberman et al., 2015; Song et al, 2016).
251 Besides, it is known that cochlear ultrastructure varies along the tonotopic position
252 (Michanski et al., 2019; Payne et al., 2021), but determining precise cochlear locations of
253 the acquired EM volumes in 3D has not yet been established, hampering a reliable inter-
254 sample structural comparison. Recent work has demonstrated x-ray tomography as a
255 powerful tool for morphological study of whole cochleae and its potential to combine with

256 other optical methods (Keppeler et al, 2021; Lu et al, 2021). In the present work, we show
257 the practice of targeting given cochlear tonotopic ranges by using x-ray-tomographic
258 reconstruction to guide sample trimming and sequential SBEM imaging (Appendix Fig S1).

259 Moreover, with ever-growing tissue sizes allowed by improved sample preparation
260 (Genoud et al, 2018; Hua et al., 2021; Hua et al, 2015; Mikula & Denk, 2015) and faster EM
261 acquisition (Hua et al, 2022; Svara et al, 2022; Zheng et al, 2018), image processing has
262 become nowadays a major limitation for high-throughput connectomic and morphomic
263 investigations (Helmstaedter, 2013; Kubota et al, 2018; Varsano & Wolf, 2022). Our recent
264 work has proposed a robust analysis pipeline with full-automated segmentation for IHC
265 outer membranes, ribbon synapses and mitochondria (Liu et al., 2022). Here, we
266 demonstrate that the algorithm is readily applicable for SBEM datasets which were acquired
267 from different animals and cochlear locations (Fig 1A and Table 1). This yields a more than
268 10-fold increase in total number of the reconstructed IHCs as before, boosting
269 ultrastructural profiling of the IHCs under different experimental conditions.

270 In summary, our SBEM quantifications of the IHCs provide an extensive set of
271 observations after acoustic overexposures, including: (1) increased occurrence of large- and
272 multi-ribbon AZs, (2) IHC subtype-specific ribbon changes as well as (3) altered synaptic
273 mitochondrial network. Based on these ultrastructural insights, we gain deeper
274 understanding of the presynaptic concepts underlying activity-dependent ribbon plasticity
275 in the mature IHCs.

276

277 **Synaptopathic and Non-synaptopathic Acoustic Exposures.** Due to the non-linearity of
278 cochlear mechanics, the noise damage including consequent ribbon loss does not directly
279 relate to the magnitude of ABR threshold elevations (see review (Liberman, 2017)). Hence,

280 we calibrated the boundary conditions for synaptopathic (91 dB, 2 h) and non-synaptopathic
281 (85 dB, 2 h) exposures on the juvenile (5-6 weeks) CBA mice (Fig 1B and C) according to the
282 characteristic frequency-profiles of exposure-related ABR threshold shifts on animals at 16
283 weeks of age (Fernandez et al., 2015). Note that our juvenile mice have acquired ribbon loss
284 already after a two-hour exposure at 91 dB, which is considered non-synaptopathic for the
285 mature animal (Fernandez et al., 2015). This result is in line with early study (Kujawa &
286 Liberman, 2006) showing accelerated presbycusis in the young-exposed (4-8 weeks) but not
287 in the old-exposed (≥ 16 weeks) animals to a neuropathic noise (100-dB, 2 h). Taken
288 together, these findings corroborate that the juveniles are more vulnerable to noise-
289 induced hearing loss, both temporary and permanent ones. As permissible noise levels for
290 occupational exposure have been established in adults (Daniell et al, 2006; Davis & Clavier,
291 2017), preventive actions may be taken with a stricter guideline in school.
292
293 **Ribbon Plasticity and Maintenance in the IHCs.** It has been shown that ribbon size is of
294 functional significance by determining the pool of synaptic vesicles available for fusion and
295 tightly regulated by the presynaptic calcium channels (Frank et al, 2009; Sheets et al, 2012).
296 Although emerging 3D EM techniques have been employed to dissect the morphological
297 maturation of synaptic ribbons, ranging from late embryonic to adult stages (Michanski et
298 al., 2019; Payne et al., 2021), evidences for ribbon maintenance and activity-dependent
299 plasticity are scarce in the mature IHCs. Consistent to prior observations (Liberman et al.,
300 2015), post-exposure ribbons enlargement was observed in the 28 kHz-region (Fig 2D).
301 More importantly, the enlarged ribbons are not associated with "hollowing" cores or
302 obviously fewer tethered vesicles, arguing against a perturbed ribbon function beyond one
303 week after the overexposure. Besides, our quantifications provide emerging evidence for

304 morphological adaptation of the IHC ribbons to sensory experiences via conformational
305 changes. Higher occurrence of multi-ribbon AZs in the synaptopathic group (Fig 2E) is
306 counterintuitive, as enhanced synaptic transmission is supposed to make the ribbon
307 synapse more vulnerable due to glutamate-mediated excitotoxicity. Considering that the
308 multi-ribbon AZ is not only retained into adulthood (Hua et al., 2021; Michanski et al., 2019)
309 but also a hallmark of cochlear aging (Stamataki et al., 2006), the functional property of this
310 structural variant remains to be explored. It has been recently proposed (Michanski et al.,
311 2019) that, under the strict constrain of maximum ribbon size in mature IHC, such molecular
312 bypass may allow strengthening of individual synapse to maintain overall neurotransmission
313 level with reduced afferent contacts. In line with this notion, our observations of negatively
314 correlated ribbon number and mean size in an IHC (Hua et al., 2021) may reflect active
315 regulation on the total ribbon volume (Appendix Fig S2B), presumably by cellular
316 homeostasis of the "building block" abundance. Last but not least, enlarged and multi-
317 ribbons lead to an increased synapse heterogeneity following the noise-related
318 synaptopathy (Fig. 2F), suggesting that noise-induced IHC coding deficit is unlikely a simple
319 consequence of the selective loss of large ribbons and may involves maladaptive changes in
320 both pre- and postsynaptic structures.
321
322 **IHC Subtype-specific Ribbon Changes after Noise Exposure.** Our ultrastructural analysis
323 focuses on the 16 kHz- and 28 kHz-regions, where staggered IHCs with alternating
324 basolateral pole positions are prevalent (Yin et al., 2014). They constitute two distinct
325 morphological subpopulations: the abneural-side type-A IHCs having larger and more
326 crowded modiolar ribbons versus the neural-side type-B IHCs with exclusively large ribbons
327 gathering more on the pillar face (Liu et al., 2022). This significant feature implies that two

328 subtypes may differ in their compositions of ribbon synapses, which are tuned to different
329 physiological properties and prefer particular postsynaptic SGN subtypes (Petitpre et al.,
330 2018; Shrestha et al., 2018; Sun et al., 2018). However, it remains largely unexplored
331 whether there is a unifying concept of activity-dependent ribbon plasticity (including the
332 synaptopathy) for both IHC subtypes.

333 It is commonly believed that noise-induced ribbon loss occurs preferentially on the
334 modiolar IHC face (Liberman et al., 2015), but this rule may be limited to the basal-most
335 cochlear end, where usually a well-aligned single IHC-row is present. Our results suggest
336 that the worst-hit areas of noise insults are the IHC subregions with high ribbon density,
337 namely modiolar face of the type-A as well as pillar face of the type-B IHC (Fig 3B). In
338 addition, two IHC subtypes undergo distinct post-exposure ribbon reorganization: in the
339 type-A IHCs we observed declined modiolar ribbons, collapsed modiolar-pillar gradients in
340 ribbon size and density; the type-B IHCs simply gain enlarged pillar ribbons including multi-
341 ribbons at the cost of fewer in number, leaving the modular ribbons and the pillar-modiolar
342 gradients largely unaffected (Fig 3C and D). In our view, these IHC subtype-specific
343 differences can neither be readily explained by selective glutamate excitotoxicity on the
344 modiolar (or type *Ic* SGN) nerve terminals (Liberman et al., 2015; Shrestha et al., 2018) nor
345 the protective role of gradient efferent innervations (Boero et al, 2018; Liberman et al, 2014;
346 Maison et al, 2013). Thus, these observations argue for a more complex and IHC subtype-
347 specific ribbon plasticity following the classic glutamate-mediated damage on postsynaptic
348 terminals, presumably involving local metabolic stress induced by presynaptic- or
349 mitochondrial-Ca^{2+} influx as well as synaptic vesicle cycle, as recently showed in zebrafish
350 lateral-line hair cells (Lukasz et al, 2022). More importantly, these results challenge the use
351 of a global modiolar-pillar gradient for the IHCs in a staggered arrangement, and therefore

352 several prevailing concepts based on this simple assumption might not hold in the
353 functionally more relevant middle cochlea regions.
354
355 **Ribbon-associated Mitochondria in the IHCs.** Sustained neurotransmission at high rate is
356 metabolic demanding for nerve cells. Recent work suggests that the ribbon function is a
357 significant contributor to ATP consumption and reactive oxygen species (ROS) buildup in
358 zebrafish lateral-line hair cells (Lukasz et al., 2022), implying a crucial role of presynaptic
359 mitochondrial network in the maintenance of neurotransmission. In line with this notion, an
360 asymmetric mitochondrial distribution along the radial plane has been previously described
361 in the mammalian IHCs (Bullen et al., 2015). Further, our SBEM quantifications of the mid-
362 cochlea (Liu et al., 2022) and the 28-kHz region (this study) corroborate highly correlated
363 spatial gradients of mitochondria and ribbons inside a subcellular domain confined to 4.5 - 5
364 µm from the basolateral IHC pole (Fig 4B). This finding is significant since it provides a
365 structural cue for defining the putative ribbon-associated mitochondria (RAM). After the
366 synaptopathic exposure, the overall reduction in spatial correlation between mitochondrial
367 and ribbon gradients (Fig 4B) is presumably owing to dramatic ribbon reorganization or late-
368 onset RAM adaptive remodeling. Given that the ribbon size is tightly regulated by the
369 coupled presynaptic influx and mitochondrial uptake of Ca^{2+} (Wong et al, 2019), we attempt
370 to speculate that the altered mitochondrial morphology and basolateral distribution (Fig 4C-
371 E) may in turn shape the ribbon gradient in an activity-dependent manner. Together, these
372 results argue for a fascinating presynaptic mechanism in hosting the proper ribbon gradient
373 under normal condition, and which may also be involved in influencing, if not promoting,
374 the post-insult restoration of neurotransmission in the sensory hair cells.
375

376 **Materials and Methods**

377 **Animals.** In this study, CBA/Ca mice (male, ranging from p28 to p35) were purchased from
378 Shanghai Jihui Experimental Animal Feeding Co., Ltd. (Shanghai, China). Before experiment,
379 animals were raised in the same acoustic environment for maximum seven days.
380 Experiments were conduct at Ear Institute of Shanghai Jiao Tong university School of
381 Medicine and Shanghai Institute of Precision Medicine. All procedures were approved by
382 the Institutional Authority for Laboratory Animal Care of Shanghai Ninth People's Hospital
383 (SH9H-2020-A65-1).

384

385 **Acoustic overexposures.** The acoustic overexposure was carried out in a sound-attenuating
386 chamber (Shanghai Shino Acoustic Equipment Co. Ltd, China). Two acoustic overstimulation
387 protocols were used in this study: an octave-band of noise (8-16 kHz) at 91 or 85 dB for 2
388 hours (Fig 1B). During the exposure, awake animals were kept without restraint in 18 x 18 x
389 10 cm^3 sized cells (1 animal/cell) in a subdivided cage by barbed wires. The cage was placed
390 about directly below the horn of the loudspeaker (X4, HiVi Acoustic, Inc.) connected to a
391 sound card (US-366, TASCAM, Inc.). The octave-band waveform was custom-made (gift from
392 Prof. Bo Zhong, National Institute of Metrology, China) and real-time monitored by Adobe
393 Audition Software. Before each exposure session, the noise was calibrated to the target
394 sound pressure level using an acoustimeter (AWA6228+, Hangzhou Aihua Instruments Co.,
395 Ltd., China) placed in the cage.

396

397 **Auditory Brainstem Responses (ABRs).** ABR measurement were conducted as previously
398 described (Wang et al, 2021; Zhang et al, 2022). In brief, animals were anesthetized, and the
399 body temperature was maintained near 37°C using a regulated heating pad with a thermal

400 probe placed under the abdomen (Homeothermic Monitoring System, Harvard Apparatus,
401 US). Sound stimuli, which was generated by SigGen RP (Tucker-Davis Tech. Inc., US), were
402 delivered via a speaker (MF1, Tucker-Davis Tech. Inc., US) placed 10 cm away in front of the
403 animal's vertex. ABRs were recorded via three subdermal needle electrodes placed at the
404 animal's vertex (active electrode), left infra-auricular mastoid (reference electrode) and
405 right shoulder region (ground electrode). Signal digitalization and acquisition were done
406 with the software BioSigRZ (Tucker-Davis Tech. Inc., US). The raw signals were amplified
407 (5000x) and bandpass filtered (0.03-5 kHz). The sound level of stimulus started from 90 dB
408 SPL and was decremented in 5 dB steps to ~10 dB below threshold, that was defined as the
409 lowest stimulus needed for evoking visible responses.
410
411 **Sample Preparation.** The *en bloc* EM staining of cochlea was performed following the
412 established protocol (Lu et al., 2021). In brief, after being anesthetized with 2% isoflurane
413 inhalation, animals were decapitated, and temporal bones were dissected from both sides.
414 Under microscope, the cochleae were immediately perfused through the round and oval
415 windows with ice-cold fixative mixture containing 0.08 M cacodylate (pH 7.4, Sigma-Aldrich,
416 US), 2% paraformaldehyde (Sigma-Aldrich, US) and 2.5% glutaraldehyde (Sigma-Aldrich, US).
417 Post-fixation and sequential decalcification were carried out at 4°C by immersing in the
418 same fixative and with addition of 5% EDTA (Sigma-Aldrich, US) for 5 hours each. The
419 decalcified cochleae were then washed twice with 0.15M cacodylate buffer (pH 7.4) for 30
420 min each, and then immersed in 2% OsO_4 (Ted Pella, US), 2.5% ferrocyanide (Sigma-Aldrich,
421 US), and 2% OsO_4 at room temperature for 2, 2, and 1.5 hours, respectively. All staining
422 solutions were buffered with 0.15M cacodylate buffer (pH 7.4). After being washed with
423 0.15M cacodylate buffer and nanopore filtered water for 30 min each, the cochleae were

424 sequentially incubated in 1% freshly made and filtered thiocarbonhydrazide solution
425 (saturated aqueous solution, Sigma-Aldrich, US), 2% OsO_4 aqueous solution and lead
426 aspartate solution (0.03M, pH 5.0, adjusted by KOH) at 50°C for 1, 2 and 2 hours, with
427 immediate washing steps. For embedding, the cochleae were dehydrated through a graded
428 acetone-water mixture (50%, 75%, 90% acetone at 4°C for 30 min each) into pure acetone (3
429 times at room temperature for 30 min each). Then the dehydrated cochleae were infiltrated
430 with 1:1 mixture of acetone and Spurr resin monomer (4.1g ERL 4221, 0.95g DER 736, 5.9g
431 NSA and 1% DMAE; Sigma-Aldrich, US) at room temperature for 6 hours on a rotator,
432 followed by 1:2 mixture of acetone and resin monomer at room temperature for overnight
433 on a rotator. Infiltrated cochleae were then incubated in pure resin for 8-12 hours before
434 being placed in embedding molds (Polyscience, Germany) and incubated in a pre-warmed
435 oven at 70°C for at least 72 hours.
436
437 **Correlative X-ray Microscopy (XRM) and Serial Block-face Electron Microscopy (SBEM).** For
438 high-resolution XRM imaging of the cochlea, excess resin around cochlea was carefully
439 removed using a trimmer (TRIM2, Leica, Germany) equipped with a diamond knife head
440 (#227172, Anton Meyer & Co. Ltd). Cochlea samples were mounted upright along the
441 conical center axis on an aluminum metal rivet (3VMRS12, Gatan, UK) and scanned with an
442 XRM (Xradia 520 Versa, Carl Zeiss, Germany) at a pixel size of < 4.7 µm, source voltage 60 kV,
443 power 5 W and exposure time per radiograph 1 sec. Cochlear 3D reconstructions based on
444 acquired XRM datasets were visualized and further analyzed in 3D image processing
445 software (AMIRA, Thermo Scientific, US). Whole extent of the basilar membrane was
446 annotated with marked segments of interest using published mouse cochlear place-
447 frequency map as reference (Muller et al., 2005). After having trimmed the cochleae

448 coronally to the targeted location, we imaged (30 × 30 nm^2, 60 × 60 μm^2 per image) the
449 block-face of each sample using a SEM (Gemini300, Carl Zeiss, Germany) for *post hoc*
450 confirmation of the frequency range of the SBEM volumes.

451 The samples were remounted with the previously SEM-scanned block-face on top
452 and further trimmed down to a block size of about 800 × 800 x 500 μm^3 (xyz). Serial sections
453 were imaged using a field-emission SEM (Gemini300, Carl Zeiss) equipped with an in-
454 chamber ultramicrotome (3ViewXP, Gatan) and back-scattered electron detector (Onpoint,
455 Gatan). In total, six SBEM datasets were analyzed in this study (Fig 1A), two (M1 and M2) of
456 unexposed cochleae, as well as four (M3-4, two from each animal) of noise exposed
457 cochleae. Imaging parameters were as follows: incident electron beam energy, 2 keV; pixel
458 dwell time, 1.5-2.0 µs; pixel size, 12 nm; cutting thickness 50 nm; focal charge compensation,
459 100%; vacuum chamber pressure, ~2.8×10^{-3} mbar. Consecutively acquired slices were
460 aligned offline using cross-correlation function in MATLB (MathWorks, US) and cubed for
461 volume tracing in webKNOSSOS (Boergens et al, 2017; Hua et al., 2021).

462

463 **Reconstruction of IHC, Mitochondrion and Ribbon Synapse.** Using the previously trained
464 3D u-net models (Liu et al., 2022), the in-plane probability maps of IHCs and mitochondria
465 were generated by running the networks with a blocking-scheme. Distance-transform-
466 watershed algorithm was applied to each thresholded probability map to produce over-
467 segmented super-pixels for IHCs and mitochondria. To achieve volume reconstruction, we
468 used 3D connection algorithm to connect the 2D super-pixels and output the reconstructed
469 3D objects. From all the datasets, 112 IHCs were volume reconstructed. Automatic
470 detection and segmentation were carried out for all 115,115 associated mitochondria
471 residing in those IHCs (n=79) of the 28-kHz cochlear region (M1-4). Manual proof-reading

472 and correction were done in webKNOSSOS (Boergens et al., 2017) on the auto-
473 segmentation results of total 1710 ribbon synapses. The coronal plane of each IHC was
474 determined by two lines and its center point. The first line was parallel to one IHC row
475 which was computed by fitting a line with IHC centers on it. Another line was the principal
476 axis of each IHC computed by principal component analysis (PCA). Each IHC cell body was
477 then divided into pillar and modiolar hemispheres based on the coronal plane and with
478 individual ribbon synapses assigned objectively to either hemisphere.
479
480 **Statistical Analysis.** All data analysis and statistical tests were carried out using self-written
481 scripts and built-in functions in MATLAB (release 2021a) and the Statistics Toolbox
482 (MathWorks, Inc., US). The comparisons between groups were done using two-sample t-test
483 (*ttest2*) for Fig 1C, 2C-E, S2A-B, 3B-D, 4B3 and paired t-test (*ttest1*) for Fig S2C. The
484 distribution comparisons between groups were done using two-sample Kolmogorov-
485 Smirnov tests (*kstest2*) for Figure 2F, 4B3, 4E. The significance level of statistical tests was
486 denoted as n.s. for $p > 0.05$, * for $p < 0.05$, ** for $p < 0.01$, *** for $p < 0.001$ and **** for $p <$
487 0.0001.

ACKNOWLEDGMENTS

We thank Xu Ding and Bei Li for the help in the early stage of this work, thank Shanghai Jiao Tong University Instrumental Analysis Center for the assistant of XRM imaging. This work was supported by National Natural Science Foundation of China (82171133 to Y.H., 32171461 to H.H.), Industrial Support Fund of Huangpu District in Shanghai (XK2019011 to Y.H.), Innovative Research Team of High-Level Local Universities in Shanghai (SHSMU-ZLCX20211700), the Shanghai Key Laboratory of Translational Medicine on Ear and Nose Diseases (14DZ2260300), the Strategic Priority Research Program of Chinese Academy of Science (No. XDB32030208 to H.H.).

Author Contributions

Y.H. designed and supervised the study; Y.L. carried out the animal experiments, Y.L., J.L., S.W. and H.W. analyzed the data; J.L. and H.H. contributed the segmentation and 3D reconstruction; F.W. assisted with the EM acquisition; Y.H., Y.L., S.W. and J.L. drafted the manuscript. All authors commented on the manuscript.

Disclosure and competing Interests Statement

The authors declare no competing interests.

508 **REFERENCES**
509

510 Boergens KM, Berning M, Bocklisch T, Braunlein D, Drawitsch F, Frohnhofen J, Herold T, Otto
511 P, Rzepka N, Werkmeister T *et al* (2017) webKnossos: efficient online 3D data annotation for
512 connectomics. *Nat Methods* 14: 691-694
513 Boero LE, Castagna VC, Di Guilmi MN, Goutman JD, Elgoyhen AB, Gomez-Casati ME (2018)
514 Enhancement of the Medial Olivocochlear System Prevents Hidden Hearing Loss. *J Neurosci*
515 38: 7440-7451
516 Bullen A, Anderson L, Bakay W, Forge A (2019) Localized disorganization of the cochlear
517 inner hair cell synaptic region after noise exposure. *Biol Open* 8
518 Bullen A, West T, Moores C, Ashmore J, Fleck RA, MacLellan-Gibson K, Forge A (2015)
519 Association of intracellular and synaptic organization in cochlear inner hair cells revealed by
520 3D electron microscopy. *J Cell Sci* 128: 2529-2540
521 Chakrabarti R, Michanski S, Wichmann C (2018) Vesicle sub-pool organization at inner hair
522 cell ribbon synapses. *EMBO Rep* 19
523 Daniell WE, Swan SS, McDaniel MM, Camp JE, Cohen MA, Stebbins JG (2006) Noise exposure
524 and hearing loss prevention programmes after 20 years of regulations in the United States.
525 *Occup Environ Med* 63: 343-351
526 Davis RR, Clavier O (2017) Impulsive noise: A brief review. *Hear Res* 349: 34-36
527 Dow E, Siletti K, Hudspeth AJ (2015) Cellular projections from sensory hair cells form
528 polarity-specific scaffolds during synaptogenesis. *Genes Dev* 29: 1087-1094
529 Esterberg R, Hailey DW, Rubel EW, Raible DW (2014) ER-mitochondrial calcium flow
530 underlies vulnerability of mechanosensory hair cells to damage. *J Neurosci* 34: 9703-9719
531 Fernandez KA, Jeffers PW, Lall K, Liberman MC, Kujawa SG (2015) Aging after noise exposure:
532 acceleration of cochlear synaptopathy in "recovered" ears. *J Neurosci* 35: 7509-7520
533 Fettiplace R (2017) Hair Cell Transduction, Tuning, and Synaptic Transmission in the
534 Mammalian Cochlea. *Compr Physiol* 7: 1197-1227
535 Frank T, Khimich D, Neef A, Moser T (2009) Mechanisms contributing to synaptic Ca2+
536 signals and their heterogeneity in hair cells. *Proc Natl Acad Sci U S A* 106: 4483-4488
537 Frank T, Rutherford MA, Strenzke N, Neef A, Pangrsic T, Khimich D, Fejtova A, Gundelfinger
538 ED, Liberman MC, Harke B *et al* (2010) Bassoon and the synaptic ribbon organize Ca(2)+
539 channels and vesicles to add release sites and promote refilling. *Neuron* 68: 724-738
540 Furman AC, Kujawa SG, Liberman MC (2013) Noise-induced cochlear neuropathy is selective
541 for fibers with low spontaneous rates. *J Neurophysiol* 110: 577-586
542 Genoud C, Titze B, Graff-Meyer A, Friedrich RW (2018) Fast Homogeneous En Bloc Staining
543 of Large Tissue Samples for Volume Electron Microscopy. *Front Neuroanat* 12: 76
544 Grierson KE, Hickman TT, Liberman MC (2022) Dopaminergic and cholinergic innervation in
545 the mouse cochlea after noise-induced or age-related synaptopathy. *Hear Res* 422: 108533
546 Hashimoto S, Kimura RS, Takasaka T (1990) Computer-aided three-dimensional
547 reconstruction of the inner hair cells and their nerve endings in the guinea pig cochlea. *Acta*
548 *Otolaryngol* 109: 228-234
549 Heil P, Peterson AJ (2015) Basic response properties of auditory nerve fibers: a review. *Cell*
550 *Tissue Res* 361: 129-158
551 Helmstaedter M (2013) Cellular-resolution connectomics: challenges of dense neural circuit
552 reconstruction. *Nat Methods* 10: 501-507

553 Hickman TT, Hashimoto K, Liberman LD, Liberman MC (2020) Synaptic migration and
554 reorganization after noise exposure suggests regeneration in a mature mammalian cochlea.
555 *Sci Rep* 10: 19945
556 Hua Y, Ding X, Wang H, Wang F, Lu Y, Neef J, Gao Y, Moser T, Wu H (2021) Electron
557 Microscopic Reconstruction of Neural Circuitry in the Cochlea. *Cell Rep* 34: 108551
558 Hua Y, Laserstein P, Helmstaedter M (2015) Large-volume en-bloc staining for electron
559 microscopy-based connectomics. *Nat Commun* 6: 7923
560 Hua Y, Loomba S, Pawlak V, Voit KM, Laserstein P, Boergens KM, Wallace DJ, Kerr JND,
561 Helmstaedter M (2022) Connectomic analysis of thalamus-driven disinhibition in cortical
562 layer 4. *Cell Rep* 41: 111476
563 Huet A, Batrel C, Wang J, Desmadryl G, Nouvian R, Puel JL, Bourien J (2019) Sound Coding in
564 the Auditory Nerve: From Single Fiber Activity to Cochlear Mass Potentials in Gerbils.
565 *Neuroscience* 407: 83-92
566 Joselevitch C, Zenisek D (2020) Direct Observation of Vesicle Transport on the Synaptic
567 Ribbon Provides Evidence That Vesicles Are Mobilized and Prepared Rapidly for Release. *J*
568 *Neurosci* 40: 7390-7404
569 Kantardzhieva A, Liberman MC, Sewell WF (2013) Quantitative analysis of ribbons, vesicles,
570 and cisterns at the cat inner hair cell synapse: correlations with spontaneous rate. *J Comp*
571 *Neurol* 521: 3260-3271
572 Keppeler D, Kampshoff CA, Thirumalai A, Duque-Afonso CJ, Schaeper JJ, Quilitz T,
573 Topperwien M, Vogl C, Hessler R, Meyer A *et al* (2021) Multiscale photonic imaging of the
574 native and implanted cochlea. *Proc Natl Acad Sci U S A* 118
575 Kubota Y, Sohn J, Kawaguchi Y (2018) Large Volume Electron Microscopy and Neural
576 Microcircuit Analysis. *Front Neural Circuits* 12: 98
577 Kujawa SG, Liberman MC (2006) Acceleration of age-related hearing loss by early noise
578 exposure: evidence of a misspent youth. *J Neurosci* 26: 2115-2123
579 Kujawa SG, Liberman MC (2009) Adding insult to injury: cochlear nerve degeneration after
580 "temporary" noise-induced hearing loss. *J Neurosci* 29: 14077-14085
581 Kujawa SG, Liberman MC (2015) Synaptopathy in the noise-exposed and aging cochlea:
582 Primary neural degeneration in acquired sensorineural hearing loss. *Hear Res* 330: 191-199
583 Lauer AM, Fuchs PA, Ryugo DK, Francis HW (2012) Efferent synapses return to inner hair
584 cells in the aging cochlea. *Neurobiol Aging* 33: 2892-2902
585 Liberman LD, Suzuki J, Liberman MC (2015) Dynamics of cochlear synaptopathy after
586 acoustic overexposure. *J Assoc Res Otolaryngol* 16: 205-219
587 Liberman LD, Wang H, Liberman MC (2011) Opposing gradients of ribbon size and AMPA
588 receptor expression underlie sensitivity differences among cochlear-nerve/hair-cell
589 synapses. *J Neurosci* 31: 801-808
590 Liberman MC (2017) Noise-induced and age-related hearing loss: new perspectives and
591 potential therapies. *F1000Res* 6: 927
592 Liberman MC, Dodds LW, Pierce S (1990) Afferent and efferent innervation of the cat
593 cochlea: quantitative analysis with light and electron microscopy. *J Comp Neurol* 301: 443-
594 460
595 Liberman MC, Liberman LD, Maison SF (2014) Efferent feedback slows cochlear aging. *J*
596 *Neurosci* 34: 4599-4607
597 Lioudyno M, Hiel H, Kong JH, Katz E, Waldman E, Parameshwaran-Iyer S, Glowatzki E, Fuchs
598 PA (2004) A "synaptoplasmic cistern" mediates rapid inhibition of cochlear hair cells. *J*
599 *Neurosci* 24: 11160-11164

600 Liu J, Wang S, Lu Y, Wang H, Wang F, Qiu M, Xie Q, Han H, Hua Y (2022) Aligned Organization
601 of Synapses and Mitochondria in Auditory Hair Cells. *Neurosci Bull* 38: 235-248
602 Lu Y, Wang F, Wang H, Bastians P, Hua Y (2021) Large-scale 3D imaging of mouse cochlea
603 using serial block-face scanning electron microscopy. *STAR Protoc* 2: 100515
604 Lukasz D, Beirl A, Kindt K (2022) Chronic neurotransmission increases the susceptibility of
605 lateral-line hair cells to ototoxic insults. *Elife* 11
606 Lysakowski A, Goldberg JM (1997) A regional ultrastructural analysis of the cellular and
607 synaptic architecture in the chinchilla cristae ampullares. *J Comp Neurol* 389: 419-443
608 Maison SF, Usubuchi H, Liberman MC (2013) Efferent feedback minimizes cochlear
609 neuropathy from moderate noise exposure. *J Neurosci* 33: 5542-5552
610 Meyer AC, Frank T, Khimich D, Hoch G, Riedel D, Chapochnikov NM, Yarin YM, Harke B, Hell
611 SW, Egner A *et al* (2009) Tuning of synapse number, structure and function in the cochlea.
612 *Nat Neurosci* 12: 444-453
613 Michanski S, Smaluch K, Steyer AM, Chakrabarti R, Setz C, Oestreicher D, Fischer C, Mobius
614 W, Moser T, Vogl C *et al* (2019) Mapping developmental maturation of inner hair cell ribbon
615 synapses in the apical mouse cochlea. *Proc Natl Acad Sci U S A* 116: 6415-6424
616 Mikula S, Denk W (2015) High-resolution whole-brain staining for electron microscopic
617 circuit reconstruction. *Nat Methods* 12: 541-546
618 Moser T, Grabner CP, Schmitz F (2020) Sensory Processing at Ribbon Synapses in the Retina
619 and the Cochlea. *Physiol Rev* 100: 103-144
620 Muller M, von Hunerbein K, Hoidis S, Smolders JW (2005) A physiological place-frequency
621 map of the cochlea in the CBA/J mouse. *Hear Res* 202: 63-73
622 Pangrsic T, Singer JH, Koschak A (2018) Voltage-Gated Calcium Channels: Key Players in
623 Sensory Coding in the Retina and the Inner Ear. *Physiol Rev* 98: 2063-2096
624 Payne SA, Joens MS, Chung H, Skigen N, Frank A, Gattani S, Vaughn K, Schwed A, Nester M,
625 Bhattacharyya A *et al* (2021) Maturation of Heterogeneity in Afferent Synapse
626 Ultrastructure in the Mouse Cochlea. *Front Synaptic Neurosci* 13: 678575
627 Petitpre C, Wu H, Sharma A, Tokarska A, Fontanet P, Wang Y, Helmbacher F, Yackle K,
628 Silberberg G, Hadjab S *et al* (2018) Neuronal heterogeneity and stereotyped connectivity in
629 the auditory afferent system. *Nat Commun* 9: 3691
630 Safieddine S, El-Amraoui A, Petit C (2012) The auditory hair cell ribbon synapse: from
631 assembly to function. *Annu Rev Neurosci* 35: 509-528
632 Sergeyenko Y, Lall K, Liberman MC, Kujawa SG (2013) Age-related cochlear synaptopathy: an
633 early-onset contributor to auditory functional decline. *J Neurosci* 33: 13686-13694
634 Sheets L, Kindt KS, Nicolson T (2012) Presynaptic CaV1.3 channels regulate synaptic ribbon
635 size and are required for synaptic maintenance in sensory hair cells. *J Neurosci* 32: 17273-
636 17286
637 Shi L, Chang Y, Li X, Aiken SJ, Liu L, Wang J (2016) Coding Deficits in Noise-Induced Hidden
638 Hearing Loss May Stem from Incomplete Repair of Ribbon Synapses in the Cochlea. *Front*
639 *Neurosci* 10: 231
640 Shrestha BR, Chia C, Wu L, Kujawa SG, Liberman MC, Goodrich LV (2018) Sensory Neuron
641 Diversity in the Inner Ear Is Shaped by Activity. *Cell* 174: 1229-1246 e1217
642 Song Q, Shen P, Li X, Shi L, Liu L, Wang J, Yu Z, Stephen K, Aiken S, Yin S *et al* (2016) Coding
643 deficits in hidden hearing loss induced by noise: the nature and impacts. *Sci Rep* 6: 25200
644 Spicer SS, Qu C, Smythe N, Schulte BA (2007) Mitochondria-activated cisternae generate the
645 cell specific vesicles in auditory hair cells. *Hear Res* 233: 40-45

646 Spicer SS, Thomopoulos GN, Schulte BA (1999) Novel membranous structures in apical and
647 basal compartments of inner hair cells. *J Comp Neurol* 409: 424-437
648 Stamataki S, Francis HW, Lehar M, May BJ, Ryugo DK (2006) Synaptic alterations at inner
649 hair cells precede spiral ganglion cell loss in aging C57BL/6J mice. *Hear Res* 221: 104-118
650 Sun S, Babola T, Pregernig G, So KS, Nguyen M, Su SM, Palermo AT, Bergles DE, Burns JC,
651 Muller U (2018) Hair Cell Mechanotransduction Regulates Spontaneous Activity and Spiral
652 Ganglion Subtype Specification in the Auditory System. *Cell* 174: 1247-1263 e1215
653 Svara F, Forster D, Kubo F, Januszewski M, Dal Maschio M, Schubert PJ, Kornfeld J, Wanner
654 AA, Laurell E, Denk W *et al* (2022) Automated synapse-level reconstruction of neural circuits
655 in the larval zebrafish brain. *Nat Methods*
656 Vaithianathan T, Henry D, Akmentin W, Matthews G (2016) Nanoscale dynamics of synaptic
657 vesicle trafficking and fusion at the presynaptic active zone. *Elife* 5
658 Varsano N, Wolf SG (2022) Electron microscopy of cellular ultrastructure in three
659 dimensions. *Curr Opin Struct Biol* 76: 102444
660 Wang H, Li B, Lu Y, Han K, Sheng H, Zhou J, Qi Y, Wang X, Huang Z, Song L *et al* (2021) Real-
661 time threshold determination of auditory brainstem responses by cross-correlation analysis.
662 *iScience* 24: 103285
663 Wong AB, Rutherford MA, Gabrielaitis M, Pangrsic T, Gottfert F, Frank T, Michanski S, Hell S,
664 Wolf F, Wichmann C *et al* (2014) Developmental refinement of hair cell synapses tightens
665 the coupling of Ca2+ influx to exocytosis. *EMBO J* 33: 247-264
666 Wong HC, Zhang Q, Beirl AJ, Petralia RS, Wang YX, Kindt K (2019) Synaptic mitochondria
667 regulate hair-cell synapse size and function. *Elife* 8
668 Wu PZ, Liberman LD, Bennett K, de Gruttola V, O'Malley JT, Liberman MC (2019) Primary
669 Neural Degeneration in the Human Cochlea: Evidence for Hidden Hearing Loss in the Aging
670 Ear. *Neuroscience* 407: 8-20
671 Yin Y, Liberman LD, Maison SF, Liberman MC (2014) Olivocochlear innervation maintains the
672 normal modiolar-pillar and habenular-cuticular gradients in cochlear synaptic morphology. *J*
673 *Assoc Res Otolaryngol* 15: 571-583
674 Zhang Y, Lin G, Wang Y, Xue N, Lin X, Du T, Xiong W, Song L (2022) Prestin derived OHC
675 surface area reduction underlies age-related rescaling of frequency place coding. *Hear Res*
676 423: 108406
677 Zheng Z, Lauritzen JS, Perlman E, Robinson CG, Nichols M, Milkie D, Torrens O, Price J, Fisher
678 CB, Sharifi N *et al* (2018) A Complete Electron Microscopy Volume of the Brain of Adult
679 Drosophila melanogaster. *Cell* 174: 730-743 e722
680
681

Tables

Table 1. SBEM datasets from four CBA mice

	M1	M2	M3	M3	M4	M4
Sex & Age	Male, from p42 to p35					
Noise exposure	no	no	8-16 kHz, 91dB		8-16 kHz, 91dB	
Cochlear frequency (kHz)	27.8*	28.3*	15.6	26.9	16.7	29.4
Resolution (nm^3)	12 × 12 × 50	12 × 12 × 50	12 × 12 × 50	12 × 12 × 50	12 × 12 × 50	12 × 12 × 50
Volume (μm^3)	148 × 295× 154	124 × 302 × 128	177 × 268 × 109	125 × 251× 146	200 × 234 × 122	128× 360 × 139
# IHCs	15	18	16	20	17	26
# ribbons / IHC	**17.9 ± 2.0**	**16.3 ± 1.6**	**18.6 ± 2.0**	**12.5 ± 2.0**	**17.7 ± 1.5**	**11.6 ± 3.4**

*Represents the estimated value.
Data are represented as mean ± SD.

687 **Figures**

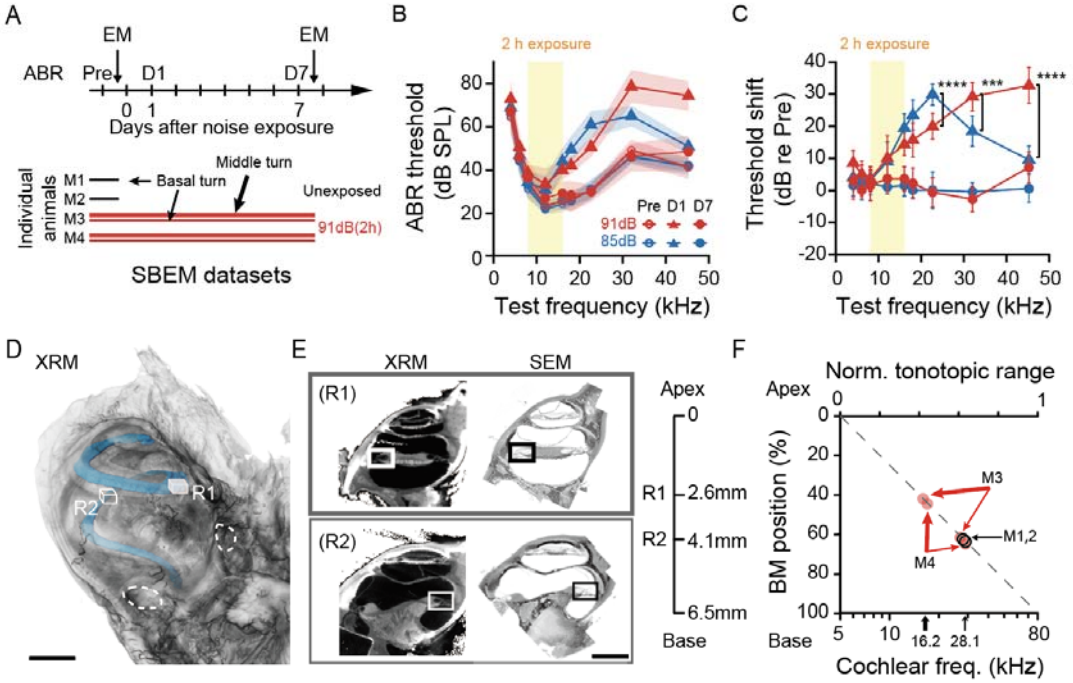

688

689 **Figure 1. SBEM imaging of the noise exposed cochleae.**

690 (A) Experimental design (top): hearing thresholds were determined by auditory brainstem
691 responses (ABRs) before (Pre), on the day-1 (D1) and the day-7 (D7) after the noise
692 exposure. Cochlea samples were collected either from the unexposed animals or on the D7
693 from the exposed ones. SBEM datasets (bottom): six EM volumes were acquired from four
694 male CBA mice (M1 to M4, p35-42) at the middle (thick line) or/and basal (thin line)
695 cochlear turns. Two were taken from the unexposed animals (M1/2, black) and the others
696 were from the animals receiving a 2-hour pure-tone (8-16 kHz) exposure at 91 dB (red,
697 M3/4).

698 (B) Both 85 dB (blue, n = 10 animals) and 91 dB (red, n = 7 animals) exposures produced a
699 transient elevation in hearing thresholds on the D1 (triangles) which was fully recovered on

700 the D7 (filled circles) in comparison with the baseline values before exposure (Pre, empty
701 circles).
702 (C) Relative ABR threshold shifts computed from (B). Different threshold shifts on the D1
703 after the 85- (blue) and the 91-dB (red) exposures at the best-frequencies of 22.6 kHz (30.00
704 ± 1.05 dB vs. 20.00 ± 0.99 dB, two-sample t-test, $p < 0.0001$), 32 kHz (18.50 ± 1.50 dB vs.
705 29.29 ± 1.09 dB, $p = 0.0003$) and 45.2 kHz (9.50 ± 1.38 dB vs. 32.86 ± 1.38 dB, $p < 0.0001$).
706 Data are presented as group means ± SEM.
707 (D) Volume rendering of reconstructed X-ray micrographs (XRM) taken from the cochlea
708 sample. Two SBEM datasets are located in the middle-turn (R1) as well as the basal-turn (R2)
709 on the cochlear basilar membrane (BM, pseudo-blue). Round window (below) and oval
710 window (right) are indicated by dashed circles. Scale bar represents 500 µm.
711 (E) Matched anatomical features between the XRM tomographic virtual sections (left) and
712 the EM images of sample block-faces (right) for targeted sample trimming and *post-hoc*
713 determination of the SBEM imaged locations (small boxes) in the middle (thick grey box)
714 and basal (thin grey box) cochlear turn. Scale bar represents 500 µm.
715 (F) Relative BM locations determined for individual SBEM volumes (the control group: black
716 circles; the 91-dB group: red dots), which were used to infer the best-frequencies of the
717 imaged IHCs based on a normalized tonotopic range from 5 to 80 kHz and yielded 16.2 ± 0.8
718 kHz and 28.1 ± 1.0 kHz for the middle (thick arrows) and basal (thin arrows) turn datasets,
719 respectively.
720

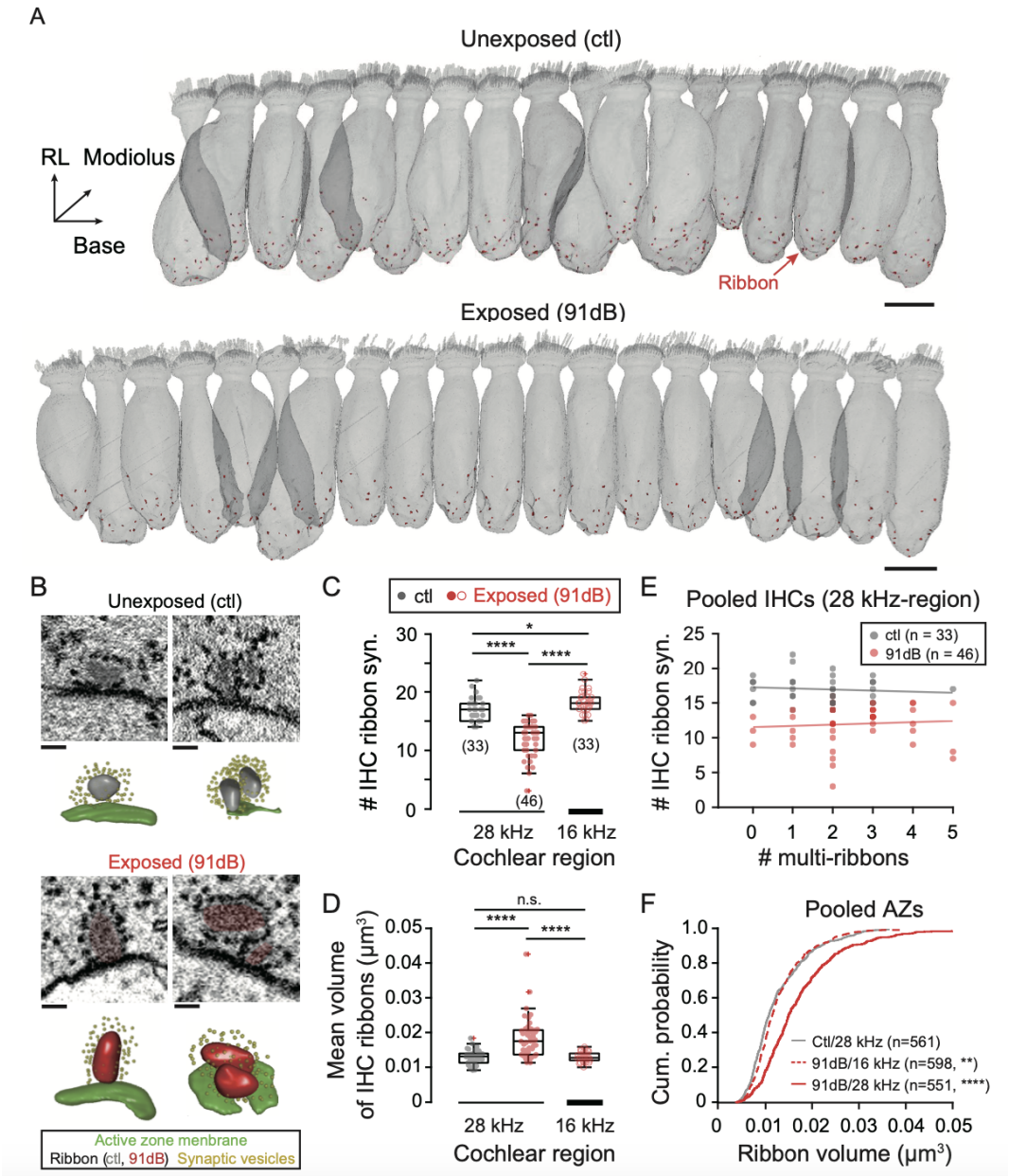

Figure 2. 3D morphological quantifications of IHC ribbons.

(A) For illustration, volume rendering of 18 reconstructed IHCs (grey) and 20 reconstructed IHCs (grey) from the control (ctl) and the exposed group (91dB) respectively. Red dots at the IHC basolateral surface represent the synaptic ribbons. Scale bar represents 20 µm.

(B) Example electron micrographs of single-ribbon (left) and multi-ribbon (right) AZs from the control (ctl) and the exposed group (91dB). For illustration, reconstructed ribbon

728 synapses including AZ membrane (green), ribbon (grey or red) and SVs (yellow) are showed
729 in 3D. Scale bars represent 0.2 μm.
730 (C) Comparisons of IHC ribbon numbers among the unexposed group (ctl, grey dots) and the
731 91-dB group (91dB, red dots). In the 28-kHz region: 17.0 ± 1.9, n = 33 IHCs (ctl); 12.0 ± 2.9, n
732 = 46 IHCs (91dB). Two-sample t-test, $p < 0.0001$ (ctl vs. 91dB). In the 16-kHz region: 18.1 ±
733 1.8, n = 33 IHCs (91dB). Two-sample t-test, $p = 0.0171$ (ctl vs. 91dB) and $p < 0.0001$ (91dB:
734 28 kHz vs. 16 kHz).
735 (D) Comparisons of mean ribbon volume per IHC among the exposed and unexposed groups.
736 In the 28-kHz region: 0.0129 ± 0.0004 μm^3, n = 33 IHCs (ctl); 0.0184 ± 0.0008 μm^3, n = 46
737 IHCs (91dB). Two-sample t-test, $p < 0.0001$ (ctl vs. 91dB). In the 16-kHz region: 0.0130 ±
738 0.0002 μm^3, n = 33 IHCs (91dB). Two-sample t-test, $p = 0.7320$ (ctl vs. 91dB) and $p < 0.0001$
739 (91dB: 28 kHz vs. 16 kHz).
740 (E) Scatterplot of number of ribbon synapses and multi-ribbons per IHC. In the 28-kHz region:
741 1.70 ± 1.19, n = 33 IHCs (ctl); 2.46 ± 1.24, n = 46 IHCs (91dB). Two-sample t-test, $p = 0.0078$
742 (ctl vs. 91dB).
743 (F) Cumulative probability distribution of ribbon size from pooled AZs in the 16-kHz and 28-
744 kHz region, respectively. The median and mean volumes of ribbons are 0.0108 μm^3 and
745 0.0128 ± 0.0064 μm^3 (ctl, n = 561 AZs), 0.0115 μm^3 and 0.0130 ± 0.0058 μm^3 (91dB: 16 kHz,
746 n = 598 AZs), 0.0151 μm^3 and 0.0174 ± 0.0092 μm^3 (91dB: 28 kHz, n = 551 AZs), respectively.
747 Two-sample Kolmogorov-Smirnov test, $p = 0.0043$ (ctl vs. 91dB: 16 kHz) and $p < 0.0001$ (ctl
748 vs. 91dB: 28 kHz). Data in 2C-D are presented as mean ± SEM. Data in 2F is presented as
749 mean ± SD.

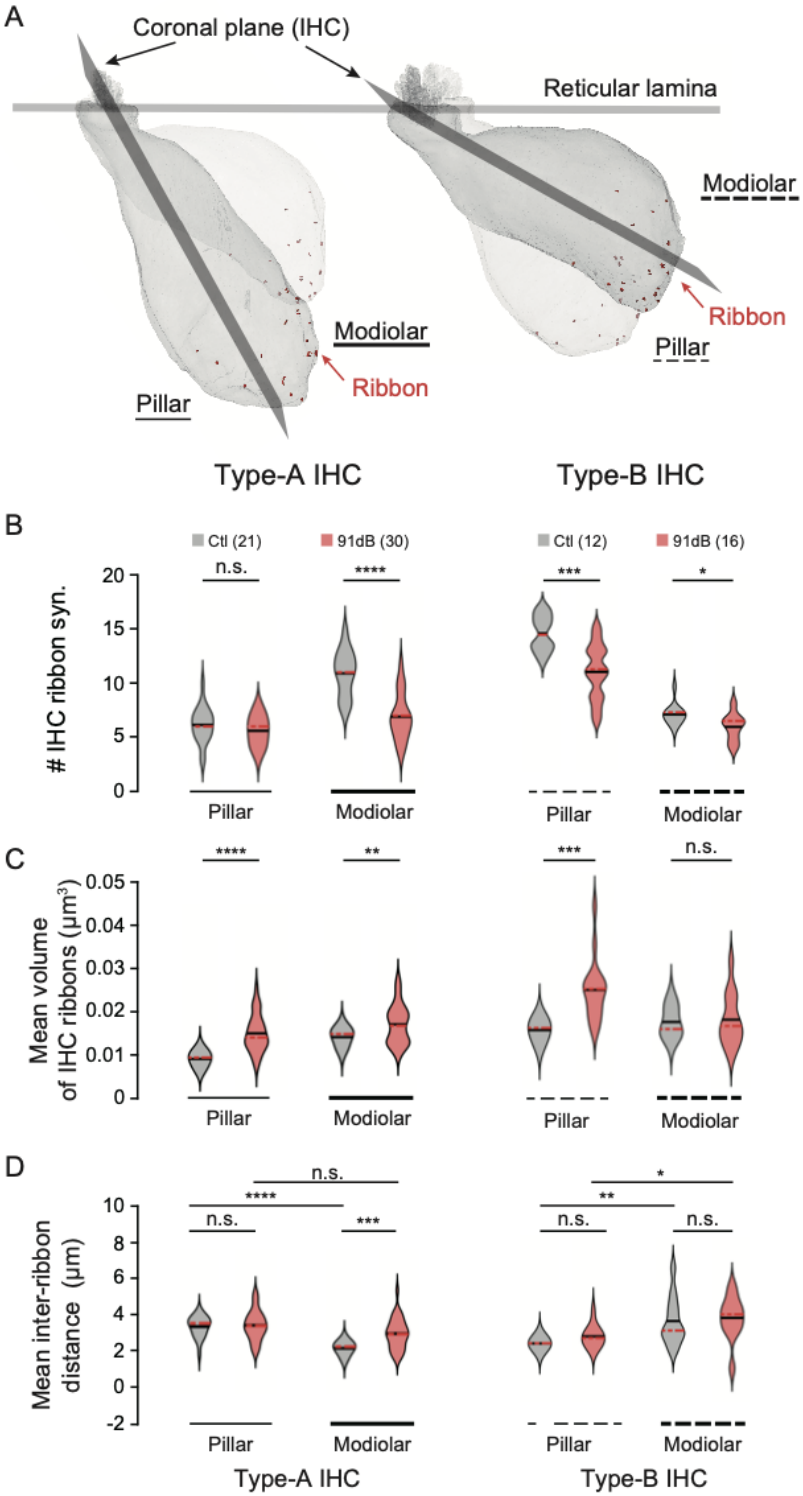

Figure 3. IHC subtype-specific, post-exposure ribbon reorganization.

(A) Example pairs of type-A (left – dark grey, right – light grey) and type-B IHCs (left – light grey, right – dark grey) are showed in sagittal view. They differ to each other by

754 characteristic tilting of the coronal plane, which divides the cell body into pillar (solid and
755 dashed thin lines) and modiolar hemispheres (solid and dashed thick lines).
756 (B) Left: comparisons of ribbon numbers in the 28-kHz region among the type-A IHCs (solid
757 lines) of different groups (grey: the control group; red: the 91-dB group). On the modiolar
758 IHC face, the ribbon numbers are 10.9 ± 2.2 (ctl, n = 21 IHCs) and 6.9 ± 2.2 (91dB, n = 30
759 IHCs). Two-sample t-test, $p < 0.0001$ (ctl vs. 91dB). Whereas there is no significant difference
760 among the pillar ribbons (ctl: 6.1 ± 1.6; 91dB: 5.6 ± 1.5). Two-sample t-test, $p = 0.2165$ (ctl vs.
761 91dB). Right: same comparison for the type-B IHCs (dashed lines). The modiolar ribbons are
762 few in number but comparable with different groups (ctl: 3.8 ± 1.2, n = 12 IHCs; 91dB: 2.3 ±
763 1.6, n = 16 IHCs, $p = 0.0145$), whereas the exposures impact on the abundance of pillar
764 ribbons significantly (ctl: 13.2 ± 2.1; 91dB: 8.7 ± 3.2). Two-sample t-test, $p = 0.0003$ (ctl vs.
765 91dB). Black and red lines represent the mean and the median, respectively.
766 (C) Comparisons of average ribbon volume in the IHCs. As for the type-A IHCs (solid lines),
767 significant ribbon enlargements occur in both modiolar and pillar IHC faces of the 91-dB
768 group (red). Modiolar ribbons: 0.0142 ± 0.0005 μm^3 (ctl, n = 21 IHCs) and 0.0171 ± 0.0008
769 μm^3 (91dB, n = 30 IHCs). Two-sample t-test, $p = 0.0088$ (ctl vs. 91dB). Pillar ribbons: 0.0091 ±
770 0.0004 μm^3 (ctl, n = 21 IHCs) and 0.0150 ± 0.0008 μm^3 (91dB, n = 30 IHCs). Two-sample t-
771 test, $p < 0.0001$ (ctl vs. 91dB). As for the type-B IHCs (dashed lines), ribbon size changes are
772 evident only on the pillar IHC face. Modiolar ribbons: 0.0153 ± 0.0011 μm^3 (ctl, n = 12 IHCs)
773 and 0.0158 ± 0.0017 μm^3 (91dB, n = 13 IHCs). Two-sample t-test, $p = 0.7963$ (ctl vs. 91dB).
774 Pillar ribbons: 0.0134 ± 0.0007 μm^3 (ctl, n = 12 IHCs) and 0.0210 ± 0.0015 μm^3 (91dB, n = 13
775 IHCs). Two-sample t-test, $p = 0.0002$ (ctl vs. 91dB).
776 (D) Comparisons of inter-ribbon distances as a measure of local ribbon density. The
777 modiolar face of type-A IHCs (thick solid line): 2.16 ± 0.08 µm (ctl, n = 21 IHCs) and 2.98 ±

778 0.16 µm (91dB, n = 30 IHCs). Two-sample t-test, p = 0.0002 (ctl vs. 91dB). The pillar face of
779 type-A IHCs (thin solid line): 3.36 ± 0.13 µm (ctl, n = 21 IHCs) and 3.44 ± 0.15 µm (91dB, n =
780 30 IHCs). Two-sample t-test, p = 0.7322 (ctl vs. 91dB). The modiolar face of type-B IHCs
781 (thick dashed line): 3.72 ± 0.38 µm (ctl, n = 12 IHCs) and 3.89 ± 0.37 µm (91dB, n = 11 IHCs).
782 Two-sample t-test, p = 0.7416 (ctl vs. 91dB). The pillar face of type-B IHCs (thin dashed line):
783 2.41 ± 0.08 µm (ctl, n = 12 IHCs) and 2.80 ± 0.18 µm (91dB, n = 11 IHCs). Two-sample t-test,
784 p = 0.0553 (ctl vs. 91dB). All data are presented as mean ± SEM.
785

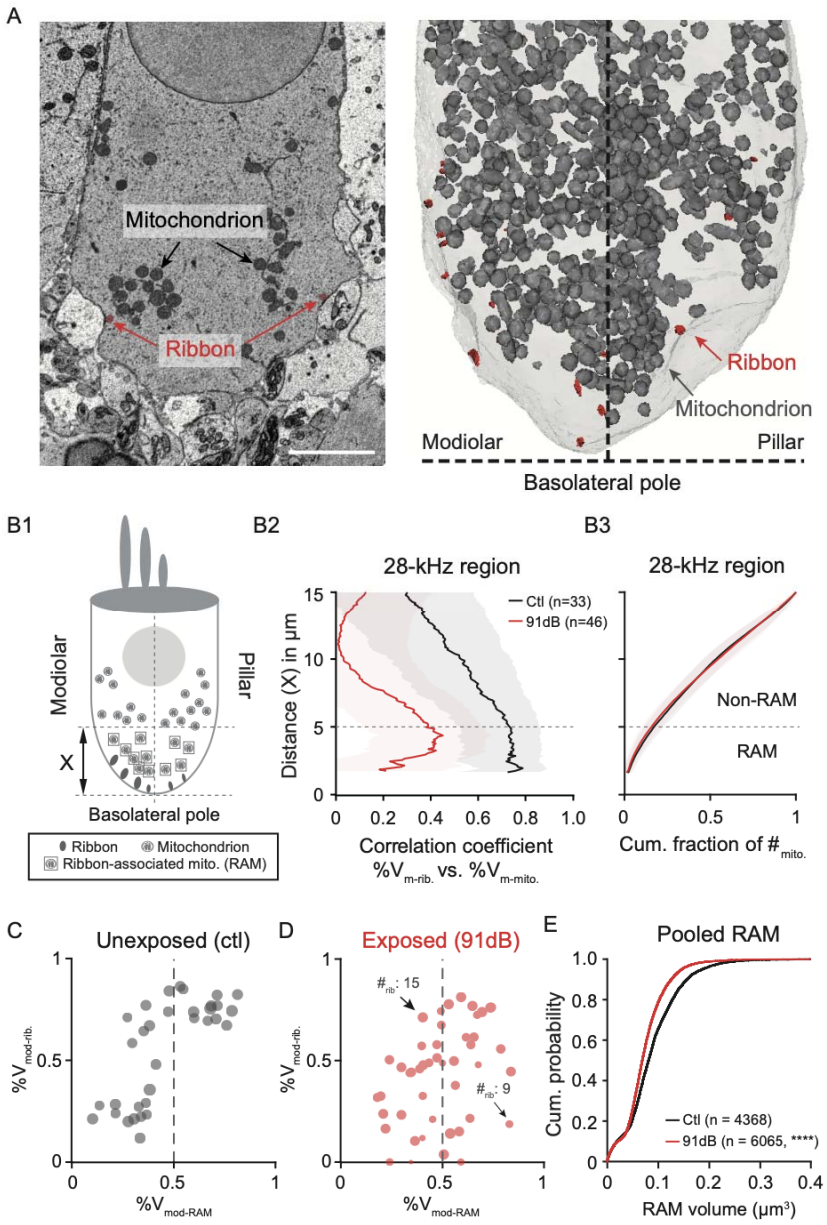

Figure 4. Activity-dependent remodeling of ribbon-associated mitochondria.

(A) Left: electron micrograph of a representative IHC (basal compartment), in which synaptic ribbons (red arrow) and mitochondria (grey arrow) are visible. Scale bar represents 5µm. Right: 3D rendering of volume reconstructed ribbons (red) and mitochondria (grey).

(B1) Schematic depicting of ribbon and mitochondrial distribution at the IHC basal compartment. With increase in the distance from the basolateral IHC pole (X), more

793 mitochondria are included in the correlation analysis with the ribbon gradient. Note that the
794 type-A and type B IHCs have opposing ribbon gradients.
795 (B2) Correlation coefficients computed between modiolar fraction of the ribbons ($\%V_{m\text{-}rib.}$)
796 and that of the mitochondria ($\%V_{m\text{-}mito.}$) within a varying distance from the IHC pole. The
797 peak correlations between ribbons and mitochondria are reached at X = 5 µm (dashed line)
798 in the control (black) and 91-dB groups (red).
799 (B3) Cumulative fraction of the mitochondrion number ($\#_{mito.}$) along the IHC middle axis
800 reveals similar radial profiles of mitochondrial distribution in the control (black) and the 91-
801 dB group (red). Number fractions of the ribbon-associated mitochondria (RAM, within 5 µm
802 from the IHC pole) are 0.1712 ± 0.0570 (ctl, n = 33 IHCs) and 0.1569 ± 0.0572 (91dB, n = 46
803 IHCs). Two-sample t-test, p = 0.2760 (ctl vs. 91dB). Two-sample Kolmogorov-Smirnov test, p
804 = 0.2400 (ctl vs. 91dB).
805 (C and D) Scatterplot of volume fraction of the modiolar ribbons with that of the RAM in the
806 unexposed (C, ctl, grey dots) and the exposed group (D, 91dB, red dots). The size of each dot
807 represents the number of ribbons per IHC.
808 (E) Cumulative fractions of pooled RAM volumes. The median and mean RAM volumes are
809 0.0808 μm^3 and 0.0882 ± 0.0542 μm^3 (ctl, n = 4368), 0.0686 μm^3 and 0.0735 ± 0.0425 μm^3
810 (91dB, n = 6065), respectively. Two-sample Kolmogorov-Smirnov test, $p < 0.0001$. (ctl vs.
811 91dB). Data in 4B are presented as mean ± SD. Black and red lines represent the mean and
812 the median, respectively.